Three-dimensional analysis of Ryugu sample particles using X-ray nanotomography.

Akira Tsuchiyama[1,2], Megumi Matsumoto[3], Junya Matsuno[1], Tomoki Nakamura[3], Takaaki Noguchi[4,5], Kentaro Uesugi[6], Akihisa Takeuchi[6], Masanori Yasutake[6], Miyake Akira[4], Shota Okumura[4], Yuri Fujioka[3], Mingqi Sun[2], Aki Takigawa[7], Toru Matsumoto[4], Satomi Enju[8], Itaru Mitsukawa[4], Yuma Enokido[3], Tomoyo Morita[3], Naoto Nakano[4] and Stefano Rubino[9], Tsukasa Nakano[10] Hisayoshi Yurimoto[11], Ryuji Okazaki[12], Hikaru Yabuta[13], Hiroshi Naraoka[12], Kanako Sakamoto[14], Shogo Tachibana[7,14], Seiichiro Watanabe[15] and Yuichi Tsuda[14], and the Hayabusa2-initial-analysis Stone and Sand teams

[1]*Research Organization of Science and Technology, Ritsumeikan University*, [2]*CAS, Guangzhou Institute of Geochemistry*, [3]*Guraduate School of Science, Tohoku University*, [4]*Guraduate School of Science, Kyoto University*, [5]*Faculty of Arts and Science, Kyushu University*, [6]*SPring8/JASRI*, [7]*Guraduate School of Science, University of Tokyo*, [8]*Guraduate School of Science and Engineering, Ehime University*, [9]*Université Paris-Saclay, CNRS, Institut d'Astrophysique Spatiale*, [10]*GSA/AIST*, [11]*Guraduate School of Science, Hokkaido University*, [12]*Guraduate School of Science, Kyushu University*, [13]*Guraduate School of Advanced Science and Engineering, Hiroshima University*, [14]*ISAS/JAXA*

We have performed initial analysis of samples returned from asteroid 162173 Ryugu by the Hayabusa2 spacecraft using synchrotron radiation-based X-ray nanotomography to elucidate the 3D structures and features of the samples with sub-micron spatial resolution as parts of the Hayabusa2 initial analysis Stone and Sand sub-teams.

We analyzed 29 and 20 particles from the first and second touchdown sites (chambers A and C), respectively. Particles of $10 \sim 150$ μm in apparent size were picked up and attached to the tips of Ti needles with Pt deposition using FIB or amorphous carbon fibers with glycol phthalate. They were imaged by two different methods (dual-energy tomography (DET) [1] and scanning-imaging X-ray microscopy (SIXM) [2]) at BL47XU of SPring-8 [3]. In DET, X-ray absorption contrast images were obtained as the spatial distribution of linear attenuation coefficient (LAC) at two different X-ray energies of 7 and 7.35 keV, which are below and above the K-absorption energy of Fe (7.11 keV), respectively. The LAC images at 7 keV correspond closely to compositional (Z) contrasts, except for Fe, and those at 7.35 keV strongly depended on Fe content. In SIXM, we obtained X-ray differential phase contrast images as the spatial distribution of refractive index decrement (RID), which is the difference between the X-ray refractive index (RI) and unity (RI = 1 - RID), at X-ray energy of 8 keV. The RID image is closely proportional to the density of the object. The voxel sizes of LAC 7 keV, LAC 7.35 keV and RID images are $47.4 \times 47.4 \times 47.4$ nm^3, $51.1 \times 51.1 \times 51.1$ nm^3 and $111.1 \times 111.1 \times 109.2$ nm^3, respectively.

The image analysis was made by combining ImageJ and codes made with C and Python. The registration among the three types of images was made with the reference of LAC 7 keV images. Then, RGB-CT images were made by assigning blue, red, and green to LAC 7 keV, LAC 7.35 keV, and RID images, respectively. Different phases including organic materials show different colors in the RGB-CT images. Minerals are quantitatively discriminated by comparing the LAC and RID values of the objects in CT images and those of minerals with known chemical compositions and densities. The solid portions of the sample particles images were extracted in LAC 7.35 keV using Chan-Base segmentation. The volume, V, surface area, S, 3-axial lengths, $A \geq B \geq C$, fractal dimension, FD, and closed porosity, p_0, were then obtained. Porosity by considering pores and cracks that are open to the outside, named as open porosity, p_∞, were also estimated by a wrapping method [4]. The density, ρ, was estimated from the averaged RID value of the particle as the lower limit. Density considering open pores, ρ_∞, was calculated as $\rho \times (1 - p_\infty)$. Sphere-equivalent diameter, D, was calculated from V and sphericity, Ψ, from V and A.

No distinct difference between the samples from chambers A and C was recognized. The sample particles are mainly composed of Mg-rich phyllosilicates (serpentine and/or saponite; Mg#~0.8-0.9) in the matrix (Fig. 1A). The phyllosilicates are not homogeneous in some particles (Fig. 1B) probably due to the difference of Mg# and/or nanoporosity below the spatial resolution. FeS (mostly pyrrhotite and minor pentlandite) grains are commonly present as hexagonal plates shown as a rectangle shape in a slice image (Fig. 1A). We found whiskers of probably FeS (Fig. 1C) in some matrices as well. Magnetite grains with different morphologies (framboidal, spherulitic, plaquette and equant) are also commonly present (Fig. 1A). Sub-micron grains of FeS and magnetite are usually present in the matrix. Dolomite is usually present mostly as aggregates of euhedral or subhedral grains (Fig. 1A) and contains minor amounts of Fe and some heavy element (possibly Mn). Aggregates of micron-sized dolomite grains are also present (Fig. 1B). Breunerite is present as a rhombohedron in shape and have the composition roughly estimated as $(Mg_{0.6}Fe_{0.4})CO_3$ (Fig. 1D). $CaCO_3$ (aragonite or calcite) is rarely present. Apatite is usually present mostly as aggregates of subhedral or anhedral grains (Fig. 1E). Small grains of forsterite or enstatite (Mg#~1) are rarely observed. Small objects (mostly <1 μm) of probably organic materials are commonly present in the matrix (Fig. 1B) but their abundance is small (probably a few % or less). Inclusions, which are empty or filled with low-Z materials, were observed in FeS, dolomite, breunerite and apatite grains (Fig. 1D). Spherical objects of phyllosilicate surrounded by fine grains of FeS

or dolomite (Fig. 1E) and object composed of Fe-rich and mostly anhydrous silicates (Fig. 1E) and fine grains of FeS and/or magnetite named "dark inclusion" (Fig. 1A) were sometimes observed. In addition to the above phases, several unidentified phases are observed as well. Some sample particles are unique; a low-density material (~ 1 g/cm^3) with a lot of fine cracks and organic-like material with embedded mineral grains. Porous objects like the ultra-porous lithology in Acfer 094 [3] were not observed.
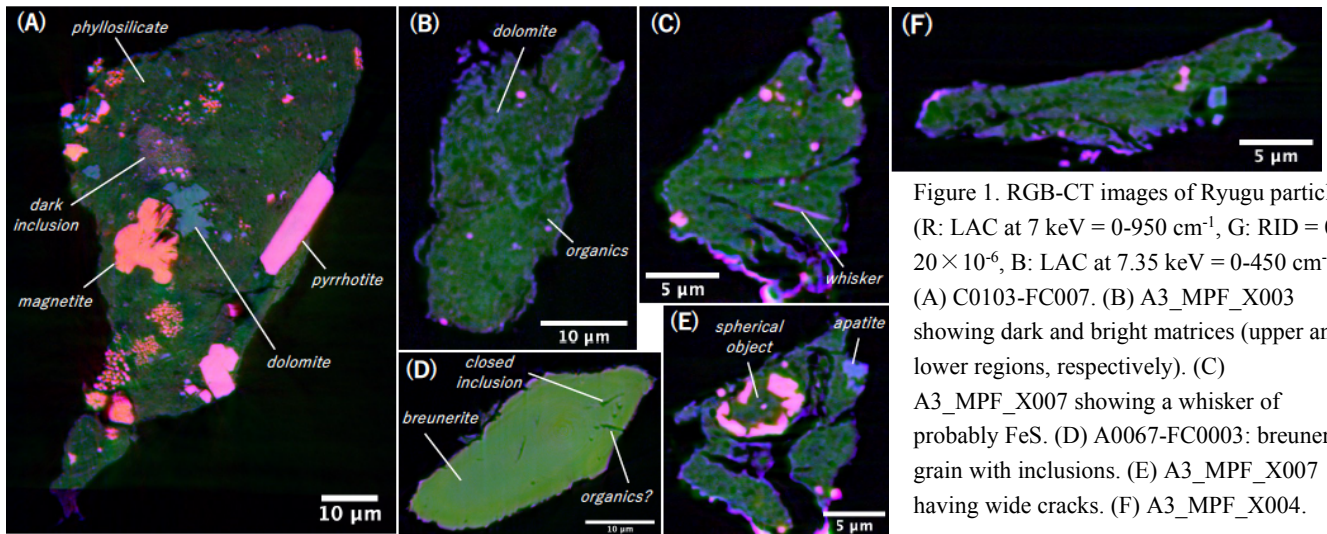

Figure 1. RGB-CT images of Ryugu particles (R: LAC at 7 keV = 0-950 cm^{-1}, G: RID = 0-20×10^{-6}, B: LAC at 7.35 keV = 0-450 cm^{-1}). (A) C0103-FC007. (B) A3_MPF_X003 showing dark and bright matrices (upper and lower regions, respectively). (C) A3_MPF_X007 showing a whisker of probably FeS. (D) A0067-FC0003: breunerite grain with inclusions. (E) A3_MPF_X007 having wide cracks. (F) A3_MPF_X004.

D ranges from 9 to 60 µm. The 3D shape distribution indicates that the Ryugu particles ($B/A =0.66$ and $C/B =0.65$ in average) are less spherical in shape than the Itokawa particles and fragments of impact experiments (*c.f.*, silver ratio: $B/A=C/B=0.71$) [1]. Some particles examined here may not be the original impact fragments on the Ryugu surface but artificial fragments during the sampling by the space craft and/or in the laboratory. Ψ is small (<0.4) and FD of some particles are <3 together with a weak correlation between them, indicating that the particle shapes are irregular and complicated. Some surfaces of the particles are convexo-concave indicating fragmentation, while some are more or less smooth and may be formed by mechanical abrasion on the asteroid as proposed for Itokawa particles [4]. Cracks less than a few µm in width are commonly present in all particles except for those composed of single crystals. Some cracks develop along the boundaries of some objects and mineral grains (Fig. 1E), implying that they are cracks formed due to shrinkage by dehydration. Some cracks are subparallel to flattened particle surfaces probably due to impact (Fig. 1F). p_0 is usually less than a few%. p_∞ mostly ranges from 5 to 20% (Fig. 2), which is less than the porosity of the CI

Figure 2. Density, ρ, estimated from the averaged RID value (lower limit) and density considering open pores, ρ_∞, plotted against open porosity, p_∞.

chondrite Orgueil (34.9% [5]). This can be explained by the different size of pores; the p_∞ counts relatively large pores ($>\sim$a few hundred nm) while that of CI counts nanopores. ρ mostly ranges from 1.3 to 1.8 g/cm^3 and and ρ_∞ from 1.1 to 1.6 g/cm^3 (Fig. 2). They are not inconsistent with the bulk density of Orgueil (1.57 g/cm^3 [5]) if we consider ρ and ρ_∞ as the lower limits.

The examined samples closely resemble CI in mineralogy and textures although we did not surely find any sulfates, such as gypsum, epsomite and blödite. The porosity and density are also consistent with those of CI. Any signature of dehydration as suggested from the IR spectrum [6] was not recognized. Highly porous materials as expected from the low thermal inertia [7] were not observed. FIB sections were prepared based on the 3D information and examined by TEM [8, 9]. The present examination is ongoing and we note that some of the ranges of physical properties, such as D, B/A, C/B, Ψ, FD, p_0, p_∞, ρ and ρ_∞, are still preliminary.

References
[1] Tsuchiyama A. et al. 2013. Geochim. Cosmochim. Acta 116;5. [2] Takeuchi A. et al. 2014. J. Synchrotron Radiat. 20:793. [3] Matsumoto M. et al. 2019. Science Advances 5;eaax5078. [4] Tsuchiyama A. et al. 2011. Science 333;1125. [5] Flynn G. J. et al. 2018. Chemie der Erde 78: 269. [6] Kitazato K. et al. 2019. Science 268:272. [7] Okada T. et al. 2020. Nature 579:518. [8] Nakamura T. et al. 2021. Abstract in this volume. [9] Noguchi T. et al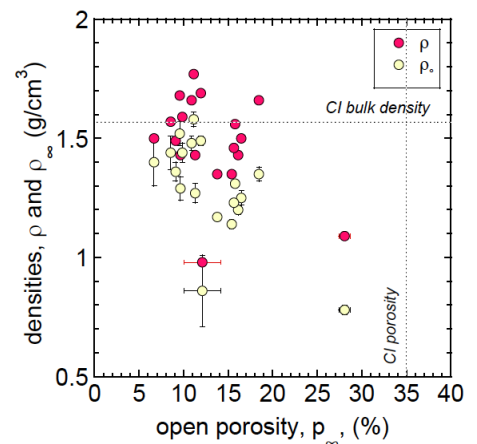. 2021. Abstract in this volume.